



# 3-D reconstruction of the atomic positions in a simulated gold nanocrystal based on discrete tomography: Prospects of atomic resolution electron tomography

J.R. Jinschek<sup>a,\*</sup>, K.J. Batenburg<sup>b</sup>, H.A. Calderon<sup>c</sup>,  
R. Kilaas<sup>d</sup>, V. Radmilovic<sup>e</sup>, C. Kisielowski<sup>e</sup>

<sup>a</sup>Virginia Tech, Institute for Critical Technology and Applied Science (ICTAS)/Materials Science and Engineering (MSE),  
309 Holden Hall (0237), Blacksburg, VA 24061, USA

<sup>b</sup>Vision Lab, University of Antwerp, Universiteitsplein 1, B-2610 Wilrijk, Belgium

<sup>c</sup>Dept. de Ciencia de Materiales, ESFM-IPN, Mexico D.F., Mexico

<sup>d</sup>Total Resolution LLC, Berkeley, CA 94707, USA

<sup>e</sup>Ernest Orlando Lawrence Berkeley National Laboratory (LBNL), National Center for Electron Microscopy (NCEM),  
1 Cyclotron Road MS 72R0150, Berkeley, CA 94720, USA

Received 8 February 2007; received in revised form 28 September 2007; accepted 10 October 2007

## Abstract

A novel reconstruction procedure is proposed to achieve atomic resolution in electron tomography. The method exploits the fact that crystals are discrete assemblies of atoms (atomicity). This constraint enables us to obtain a three-dimensional (3-D) reconstruction of test structures from less than 10 projections even in the presence of noise and defects. Phase contrast transmission electron microscopy (TEM) images of a gold nanocrystal were simulated in six different zone axes. The discrete number of atoms in every column is determined by application of the channelling theory to reconstructed electron exit waves. The procedure is experimentally validated by experiments with gold samples. Our results show that discrete tomography recovers the shape of the particle as well as the position of its 309 atoms from only three projections.

Experiments on a nanocrystal that contains several missing atoms, both on the surface and in the core of the nanocrystal, while considering a high noise level in each simulated image were performed to prove the stability of the approach to reconstruct defects. The algorithm is well capable of handling structural defects in a highly noisy environment, even if this causes atom count “errors” in the projection data.

© 2007 Elsevier B.V. All rights reserved.

PACS: 42.30.Wb; 42.30.Rx; 61.46.Hk; 68.37.Lp

**Keywords:** Atomic resolution electron tomography; Discrete tomography; Image simulation; Exit wave reconstruction; Electron crystallography; Gold nanocrystal; Tilt experiment

## 1. Introduction

Today, electron tomography is a very valuable technique in materials science to investigate the shape and structure of nanomaterials [1–6]. Efficient reconstruction algo-

rithms are available that are capable of making accurate tomographic reconstructions. A large number of projections (100–150) are needed and samples must be rotated in steps of 1–2° to create a single or dual axis tomography tilt series [7–9]. By now, the spatial resolution of such methods, that commonly utilize back projection schemes for the reconstruction, is around 1 nm<sup>3</sup> [1,3].

Preferred imaging modes involve Z-contrast methods such as high-angle annular dark field scanning transmission

\*Corresponding author. Now at FEI Company, Eindhoven (NL).

Tel.: +1 540 231 0479; fax: +1 540 231 3386.

E-mail address: [jrjinschek@gmail.com](mailto:jrjinschek@gmail.com) (J.R. Jinschek).

electron microscopy (HAADF-STEM) [1] and annular dark field transmission electron microscopy (ADF TEM) [5] or phase contrast methods [10,11]. These approaches usually avoid zone axis sample orientations in order to minimize non-linear intensity contributions caused by dynamic electron scattering and by electron channelling. Nevertheless, ignoring high symmetry zone axis orientations implies reducing the resolution of the tomographic reconstruction.

On the other hand it is desirable to exploit the atomic resolution capability of scanning/transmission electron microscopes (S/TEM), which benefits from dynamic scattering. However, it is impossible to record zone axis images every  $1-2^\circ$  because suitable zones do not occur that frequently. Therefore, data acquisition and tomographic reconstruction must necessarily differ from present techniques.

In this paper, we propose a novel method that utilizes only zone axis crystal orientations and, thereby, exploits dynamic scattering effects. We make use of the high spatial resolution of transmission electron microscopes and an improved signal-to-noise ratio (S/N) for the detection of single atoms in order to accurately reconstruct the three-dimensional (3-D) location of all atoms in a gold nanocrystal test structure with atomic resolution, and thereby its size and shape.

Atomic resolution tomography represents an enormous challenge. The intensity in a high-resolution image must be quantified. The microscope must have single atom detectability in order to determine the thickness of the atomic columns as well as the capability to tilt the sample between major zone axes.

Potential paths to register single atoms in 3-D electron microscopy were discussed as early as 1974 [12,13] but could not take into account the full complexity of dynamic electron scattering. In this approach, the samples often degrade because of their long exposure to the electron beam [13] during the acquisition of the required 100–150 projections. Miao et al. [14] have suggested atomic resolution 3-D electron diffraction microscopy by combining coherent electron diffraction with the oversampling phasing method. Without utilization of prior knowledge, they determined the 3-D structure of a nanocrystal with a resolution of 1 Å from simulated diffraction patterns, which they distorted by noise. Wu et al. [15] recently proposed to employ lens-less imaging for the reconstruction of the samples geometry from diffraction patterns. Similarly, Zuo et al. [16] experimentally reconstructed the image of a nanotube from a diffraction pattern.

On the other hand, there is prior knowledge available that links to the very nature of crystalline systems, namely that crystals often consist of only a few different elements and that the atoms are arranged on a regular grid. Obviously, it would be preferable to use as little prior knowledge as possible about the structure of the sample, as there is always the risk of making wrong assumptions. However, high-resolution images can only be obtained

along a small number of zone axes, separated by large angles. Because the number of available projection images is too small for conventional electron tomography, the reconstruction algorithm needs to use prior information to be effective.

Our approach exploits the fact that crystals are discrete assemblies of atoms (atomicity). The algorithm that we use for the reconstruction [17,18] has been developed in the field of discrete tomography (DT), which deals with the reconstruction of images containing only a few different pixel values [19,20]. In this paper, we deal with binary (i.e., black-and-white) images, where a white pixel (or “voxel”, in the case of a 3-D volume) corresponds to the presence of an atom (or “1”) at a certain position in the lattice and a black pixel corresponds to an unoccupied position (or “0”). Contrary to conventional tomography algorithms, which can be used for any kind of sample, DT algorithms are highly specific, as they are designed to incorporate as much problem-specific knowledge as possible. This typically requires far fewer projections compared to conventional tomography.

The outline of this paper is as follows. Section 2 briefly reviews approaches for single atom detection in electron microscopy. This is the postulate for our DT approach, which requires the ability to detect single atoms in the projection images of a nanocrystal obtained along different zone axes. Section 3 provides an introduction to DT and explains how it can be used to compute a 3-D reconstruction of a nanocrystal from its zone axis projections.

Although our reconstruction procedure is a general approach for reconstructing crystalline nanostructures in 3-D, a cube–octahedron gold nanocrystal is used in our simulation experiments. Gold has the advantage that the crystal structure, even on the nanoscale, is well-explored, making it perfectly suitable for validation experiments. The ability to reconstruct nanoscale (gold) particles in size and shape with atomic resolution, especially if they include defects, is already important by itself, which we motivate in Section 4.

The following part focuses on our preliminary experimental findings. We demonstrate in a first discrete tilt experiment that it is feasible to determine exit wave images of a gold nanostructure in several different zone axis projections using two tilt axes (Section 5). In Section 5.2, we generate a discrete dataset by atom counting from complex exit waves from a few-nanometer-sized gold nanocrystal. Such waves are determined from simulated through-focus HRTEM images in six different zone axes and with the parameters of specific microscopes. Section 5.3 describes the computation of a 3-D reconstruction of the cube–octahedral nanoparticle by applying the algorithm of DT and using the simulated projection data. How our reconstruction approach handles data of a nanocrystal that contains several defects is considered in Section 5.4. In Section 5.5, we test the stability of our approach by considering atom count errors in the projection data that may occur under extreme noise

conditions. In both cases, with and without defects, experimental noise has been considered in the simulation experiments. Finally, we summarize our approach and draw final conclusions.

## 2. Single atom detection in electron microscopy

The development of QUANTITEM can be considered as the first attempt to reconstruct a sample volume from the 2-D intensity distribution of electron micrographs [21–23]. At that time, 3-D atomic resolution could not be achieved for reasons that are understood today; lens aberrations, microscope instabilities, and a limited detector performance hampered the detection of single atoms, which is a crucial requirement for the development of electron tomography with atomic resolution. Many of these shortcomings were addressed during the last decade. In the first place, the development and improvement of field-emission gun (FEG) have made possible to produce a bright, coherent and intense electron source that permits correction of aberrations and thus an extended spatial resolution to sub-Ångstrom values [24,25] in these high performance transmission and scanning transmission electron microscopes. Currently, some lens aberrations can be corrected by hardware via the use of specific electron optical systems [25,26] and/or software [27,28] by determining the complex exit-wave function of an object [29–31]. Additionally, FEG electron microscopes have significantly increased microscope sensitivity in terms of a better S/N for the detection of single atoms [32–34]. This improved S/N allows for measuring of discrete intensity steps per contributing atom in a given atom column, which was experimentally verified for a gold sample by the application of HAADF-STEM [32] and of phase contrast microscopy [33,35] (Fig. 1). The methodology to count the number of atoms in a given column, however, depends on the applied imaging mode.

Phase contrast images can be interpreted further to determine the composition of atom columns. QUANTITEM proposed a quantitative analysis of the 2-D intensity distribution of HREM images, but such an analysis lacked an important parameter, namely the electron wave exiting the sample. At present, this problem has been solved, since the complex electron exit wave function (EWF) can now be recovered reliably from recorded images [36]. This achievement has solved the phase problem, which is inherent to any imaging technique that records intensities instead of waves. Technically, this is done by holographic recording, which uses either a focal series of HRTEM images [27,37,38], a tilt series of HRTEM images [39,40] or single off-axis electron holograms [41]. In the reconstruction process, the defocus dependence of lattice image patterns is eliminated and delocalization as well as lens aberrations up to the third order can largely be reduced [42,43]. Further, the procedure extends the microscope resolution to its information limit, which can reach sub-Ångstrom values [44]. Aiming at atomic resolution electron tomography, another requirement is the ability to relate the complex

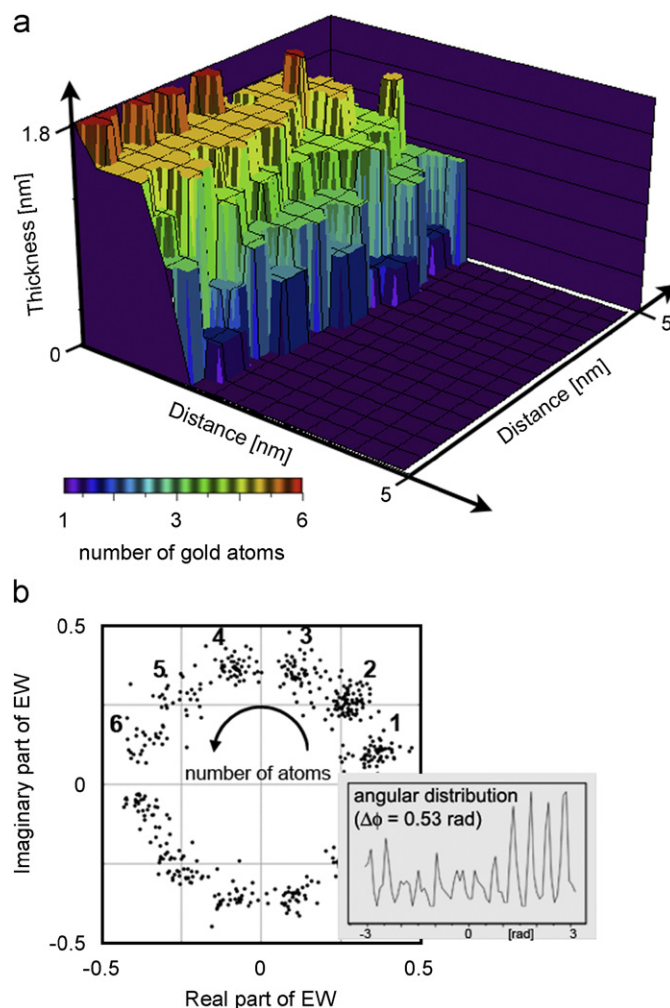


Fig. 1. (a) 3-D plot of the sample morphology of a wedge-shaped gold [1 1 0] sample, using HRTEM phase imaging (exit-wave reconstruction); and (b) channelling map (Argand diagram) of the measured exit-wave amplitude and phase values. Lower right inset: angular distribution of the experimental data showing the discrete phase change per single gold atom— $\Delta$  phase per atom  $\sim 0.6$  rad (more details in Refs. [33,35]).

EWF to the crystal structure. There are currently two approaches addressing this problem: the channelling theory [35,45] and reversed multislice calculations [46,47].

The reversed multislice algorithm utilizes a non-linear optimization scheme to determine an optimum phase grating. It employs two constraints: knowledge of the entrance wave and the experimentally measured electron EWF. Thereby, local crystal thickness and chemical composition can be determined [46,47].

The channelling theory [45] and the related S-state model [48] describe the dynamical scattering of electrons in a thin specimen by an analytical approach. In zone axis orientation and with a sufficient separation between atom columns (such as a low-index crystallographic zone axis orientation), electrons channel along the columns [35]. Instead of analyzing the total electron object exit wave  $\Psi$ , the method describes the channelling wave  $\Psi_S$  that is trapped in the atom column potential.  $\Psi_S$  relates to  $\Psi$  by

$\Psi_S = (\Psi - \Psi_v)/\Psi_v$  (with  $\Psi_v$ -vacuum electron wave) [33,35]. Several predictions of the S-state model have been verified: the amplitude of  $\Psi_S$  is strongly peaked at the atom column positions while the phase is constant over the atom column and proportional to the column “weight” which is determined by the chemical nature of the atoms and their spacing along the column direction parallel to the electron beam. The amplitude of  $\Psi_S$  oscillates periodically (sinus) as function of thickness and the phase increases linearly with thickness with a phase change per atom that is characteristic for the considered element [35,49]. Extracting amplitude and phase at the column position from  $\Psi_S$  and plotting it in the complex plane and in polar coordinates (Argand diagram: x-axis=real part of  $\Psi_S$ , y-axis=imaginary part of  $\Psi_S$  [50]) produces a “channelling map” [35,51]. The discrete nature of the channelling map directly reveals the characteristic number of atoms in each column [33,35]. The present work makes use of the channelling model to determine the number of atoms in a column.

Fig. 1a shows a reconstructed thickness map of a wedge-shaped gold [1 1 0] sample recovered from an experimental EWF (details in Ref. [33]). The corresponding channelling map is depicted in Fig. 1b. It reveals the number of gold atoms in a particular atom column. The sample thickness increases atom by atom, following a counter clockwise rotation along the circle. The angular data distribution (inset in Fig. 1b) reveals a phase change of about 0.6 rad for the scattering of the channelling electron wave single gold atom, in agreement with theoretical expectations. Consequently, single gold atoms can be recorded with a S/N between 5 and 6 with the One-Ångström Microscope (OAM) [33,35].

Single atom detection has become possible for some elements in the Periodic Table in high performance electron microscopes. The S/N of the OAM and the TEAM microscope (NCEM, Berkeley) are examples of high performance electron microscopes where single atom detection is possible. It is also very likely that single atom detection will soon become possible for most elements. Utilizing phase contrast, oxygen fluctuations have been recently imaged in a thin oxide sample by aberration corrected phase contrast microscopy [52]. On the other hand, Z-contrast microscopy discriminates better between elements because of the concave character (amplification) of the S/N curve ( $\sim Z^{1.7}$ ). Thereby, single atom sensitivity can be obtained for elements with larger  $Z$  [53]. Examples include the detection of single antimony atoms (Sb,  $Z = 51$ ) in silicon (Si,  $Z = 14$ ) [54] and the detection of a single hafnium atom (Hf,  $Z = 72$ ) at the Si/SiO<sub>2</sub> interface [55], although in this last case, the Hf atoms are not in a periodic arrangement.

In any case, these examples highlight well that it is timely to revisit electron tomography with atomic resolution: single atom detection is currently achievable for a higher number of elements and soon for most microscopes because of the ongoing instrumental improvements.

### 3. Discrete tomography

Crystalline materials have two characteristic properties that make them attractive for using DT. Firstly, the atoms in a crystal are arranged in a highly regular grid, possibly with some deviations from the perfect grid. Secondly, each grid position is either occupied or vacant: it cannot contain more than one atom and it cannot contain only a fraction of an atom.

The theoretical foundations of DT have been studied extensively since the late 1980s, motivated by the development of QUANTITEM [21–23]. It has been demonstrated that if only a small number of projections is used, it is essential to use additional prior knowledge about the structure of the sample. If no additional knowledge is incorporated, there may be many “solutions”, i.e., reconstructions that all have exactly the same projections. Gardner et al. [56] proved that even if there is only one structure that has the right projections, it may be a very difficult computational task to find this structure. Fortunately, the reconstruction is often simplified when the images are not random, but exhibit certain patterns. Exploiting this fact represents the key to creating effective reconstruction algorithms.

Several algorithms for DT on a discrete grid have been proposed in the literature [18,57,58]. Most of them have been designed to reconstruct 2-D images from 1-D projection data. Although research has been focused on algorithms for reconstructing 0–1 images, it is noted that DT techniques can also be applied when the number of pixel values is greater than two.

Recently, a new method has been developed [59] that is capable of reconstructing large 0–1 image sets ( $256 \times 256$ ) with high accuracy from a small number of projections. A further generalization of this approach to include 3-D images is used in this work [17,18]. In the experiments of Section 5.3, this algorithm is applied to simulated phase contrast (bright-field) images of a cube–octahedron gold nanocrystal. Our objective is to test and apply the concept of DT, thus obtaining atomic resolution in three dimensions.

The basic mathematical model for DT is shown in Fig. 2a for a grid of 36 positions. Occupied positions (atoms in the crystal lattice) are represented by “1”; unoccupied grid positions are represented by “0”. Fig. 2a shows the result of counting occupied position, equivalent to atom counts, in the horizontal direction. The atom count for each horizontal line can be considered as a linear equation, where the unknowns are the “pixel values” at the 36 grid positions with discrete values of either 0 or 1. Fig. 2b shows the same structure, this time depicting the atom counts in four projections (horizontal, vertical, diagonal and anti-diagonal). Again, each of the measured atom counts provides a linear equation, resulting in a system of linear equations with 34 equations and 36 unknowns. In principle, such a system has no unique solution, because the number of unknowns is larger

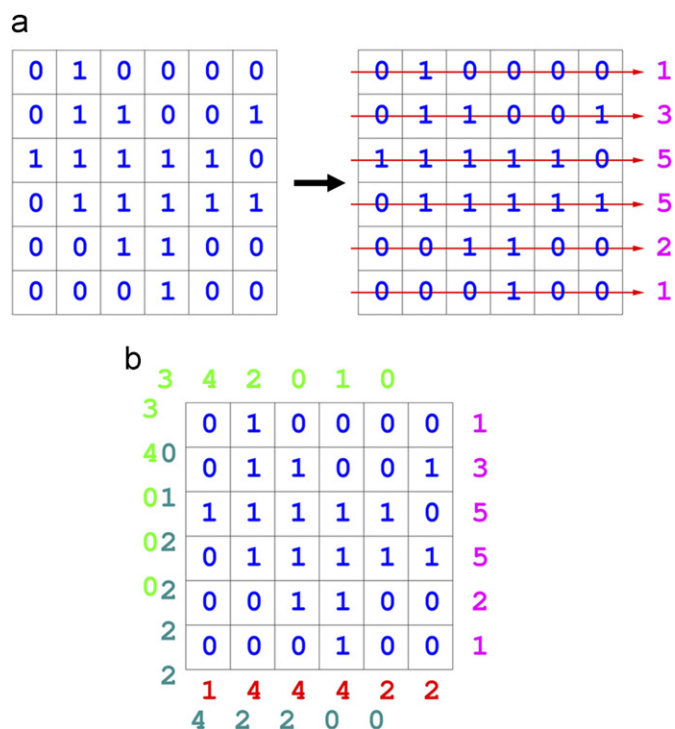


Fig. 2. Basic mathematical model of discrete tomography; occupied discrete grid positions (such as atoms in crystal lattice) are represented by “1”s, unoccupied grid positions by “0”s. (a) Determination of the atom counts (occupied grid positions) in the horizontal direction. (b) Atom counts in four projections (horizontal, vertical, diagonal and anti-diagonal). Numbers in the periphery correspond to counts along the diagonal and anti-diagonal projections.

than the number of equations. In a conventional tomographic reconstruction algorithm, any real value can be assigned to a given pixel and the system of equations has indeed an infinite number of solutions. In DT, the pixel values are restricted to binary values. Using this restriction, the reconstruction problem in Fig. 2b does have a unique solution. This shows that fewer projections are needed in this particular case using the binary constraint. The same principle holds for larger images.

In DT, the measured values correspond directly to atom counts, which can assume only integer values. This is another advantage over conventional tomography algorithm, in which the measured projection values (i.e., the pixel values of the CCD camera) are modelled as real-valued line integrals through the sample. As we will demonstrate in Section 5.4, the fact that in our DT approach all projection data are only integer-valued is advantageous for correction of atom counting errors in the projection data.

#### 4. Importance of the determination of size and shape of nanoparticles—for example: gold

In this section, we discuss the motivation to determine the size and shape of nanoparticles as well as current

limitations of other methods. The principles we discuss are general, yet we focus here on gold nanoparticles.

The field of science is more and more focused on the discovery and the synthesis of nanostructured materials as well as the understanding of the unique properties imparted by confined systems. The detailed characterization at the atomic scale plays a key role to understand size-dependent shape, surface and internal crystal structure. Specific properties of nanocrystals are determined not only by their finite size but also by their shape, defined by the crystallographic structures of the particle specific surface facets [60]. In the case of gold, it is known that the melting temperature  $T_m$  of nanoparticles strongly depends on the crystal size. For example,  $T_m$  of gold nanoparticles with a 2.5 nm diameter is ~40% lower than that of bulk gold [61]. In addition, the shape of a gold particle may change during annealing, i.e., the sublimation activation energy of Au {110} faces has been found to be significantly lower than that of {100} and {111} [62]. Barnard et al. [63,64] used first principle calculations to investigate the morphology of Au nanoparticles in the range 1–3 nm [64] and 3–100 nm [63]. Their results indicate that the equilibrium shape of fcc gold nanoparticles smaller than 1 nm is the cube–octahedron. However, this shape rapidly becomes energetically unstable with respect to the truncated octahedron, octahedron and truncated cube shapes as the size increases [64]. In the 3–100 nm range, the equilibrium shape of gold nanoparticles is a modified truncated octahedron. They also predict that the size-dependent melting behaviour of Au nanoparticles is preceded by a significant change in the morphology of the particle [63].

The precise distinction of different nanoparticle shapes in sizes smaller than the 3 nm is essential to link unique size-dependent properties. High-resolution S/TEM experiments on Au nanoparticles [60,65] have strong limitations in terms of identifying the particle shape since images correspond to 2-D projections of 3-D bodies. Ascencio et al. [65] compare experimental and simulated HRTEM images (2-D projections) in optimum defocusing condition using several zone axes to deduce the shape of gold nanoparticles. They conclude that the nanoparticles have the shape of a truncated icosahedron, which in some orientations appears as an asymmetric decahedron. However, such indirect results can always be improved by methods of tomography that can render direct information related to the size and shape of nanostructures. Recently, Arslan et al. [3] applied “conventional” electron tomography to determine the size and shape of an embedded tin/silicon quantum dot system. The spatial resolution of their method can be set at around 1 nm<sup>3</sup>. This gives rise to complications in the interpretation of the results since the crystallographic facets of the quantum dots and thus their shape can only be determined with limited accuracy (see Fig. 2 in Ref. [3]). Clearly, electron tomography with higher resolution is necessary to determine the size of nanodots and to identify their shape and the corresponding crystallographic facets, particularly for sizes lower than

3 nm. This implies determination of all atomic positions in the nanobody from 2-D projections taken in different orientations.

The objective of this paper is to apply the concept of DT to obtaining atomic resolution in three dimensions so that the size and the shape of particles can be determined precisely. Hence, for the simulation experiments we have chosen to focus on the 3-D reconstruction of a specific gold nanocrystal smaller than 3 nm. Simulation experiments are used to obtain a discrete tilt series of EWR images. Defects in the nanoparticles as well as noise are also incorporated in the experiments. Our approach is by no means limited to the reconstruction of (gold) nanocrystals, or even to the reconstruction of crystals containing a single type of atom.

We tested our approach on a cube–octahedron gold nanocrystal (size  $\sim 2.2$  nm). Fig. 3 shows the size, shape and atomic distribution of the nanocrystal used for image simulation.

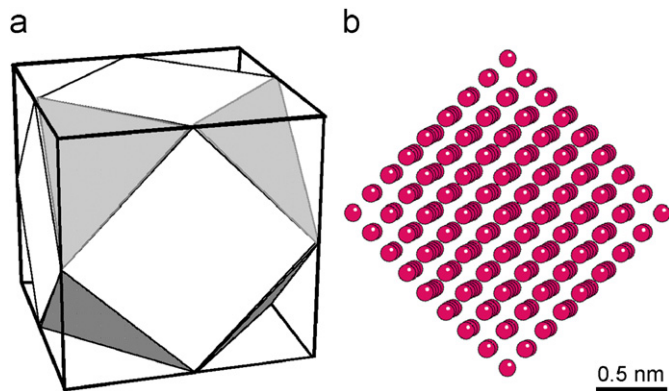


Fig. 3. (a) Cube–octahedron and (b) size, shape and atomic distribution of the nanocrystal used for image simulation.

and atomic distribution of the modelled nanocrystal. The model structure used in this simulation experiment consists of 309 atoms, arranged to form a four-shell cube–octahedron nanocrystal (for details see Refs. [66,67]). The cube–octahedron was placed in a cubic supercell with a lattice parameter of 10 nm to ensure that the particle contrast was not affected by electron scattering from the unavoidable adjacent particles generated by the periodic boundary conditions imposed by the computation.

Fig. 4a shows the three high symmetry projections ( $[001]$ ,  $[110]$ , and  $[111]$ ) of a pure gold nanocrystal as created by CrystalKit<sup>TM</sup> [68]. A total of six different zone axis orientations ( $[111]$ ,  $[1\bar{1}1]$ ,  $[001]$ ,  $[110]$ ,  $[1\bar{1}0]$ , and  $[011]$ ) are used as indicated in the Stereographic Projection given in Fig. 4b. These projections have been selected as to mimic a real tomographic experiment.

## 5. Experimental results

### 5.1. The first discrete tilt experiment—for example: gold

There is an important limitation for the acquisition of data to apply DT, i.e., the tilting capabilities of the sample holder. A piezo-driven dual-axes tomography holder for a high-resolution, large S/N environment is under development in the framework of the TEAM-project [69]. Until then the availability of a suitable holder, i.e., the limited tilt accuracy and limited tilt angle range to access necessary low-index zone axis orientations in nanocrystals, is experimentally a restriction. Nevertheless, a special double-tilt tomography holder (H. Zandbergen, TU Delft/NL, 2005)

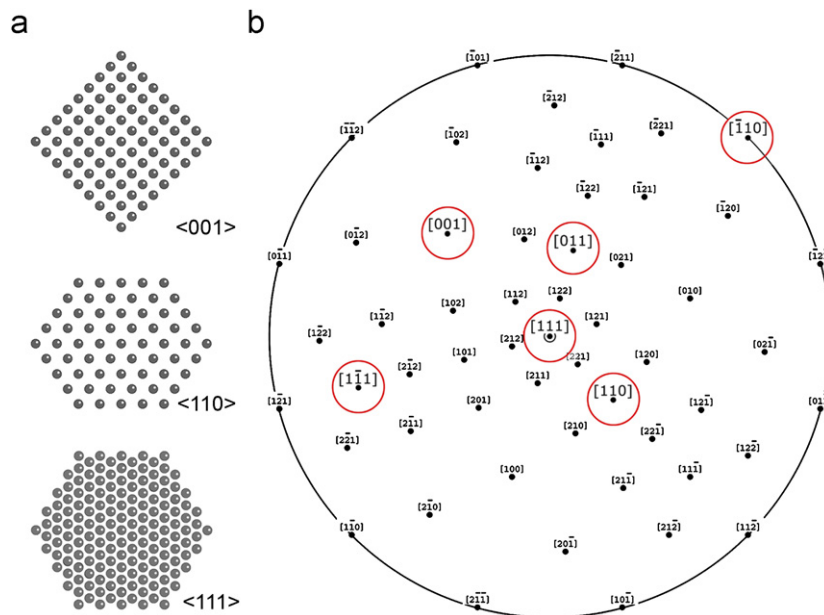


Fig. 4. (a) Projection of the atomic model of the cube–octahedron nanocrystal in three major zone axis orientations ( $[001]$ ,  $[110]$ ,  $[111]$ ). The number of atomic layers in directions perpendicular to the indicated zone axis can be counted directly. (b) Stereographic projection of a cubic crystal with six marked zone axis orientations ( $[111]$ ,  $[1\bar{1}1]$ ,  $[001]$ ,  $[110]$ ,  $[1\bar{1}0]$ ,  $[011]$ ). Exit wave functions of the nanocrystal have been simulated in these orientations to create a discrete grid input for the tomography algorithm in use.

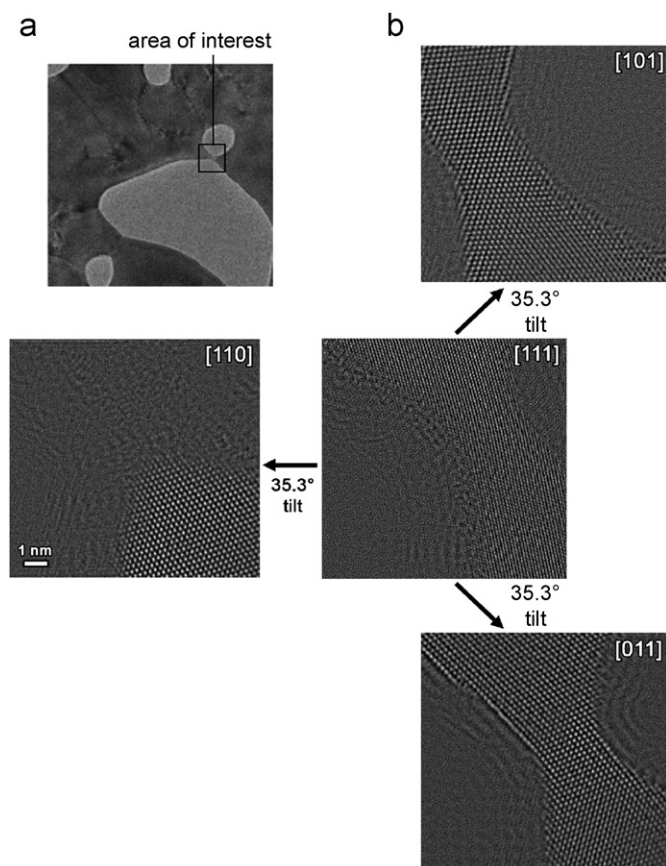


Fig. 5. Discrete tilt experiment on a thin area in a gold sample utilizing a special double-tilt tomography holder (Zandbergen, 2005) in a high-resolution, highly sensitive environment (UT lens of Berkeley's OAM microscope). (a) Overview showing the area of interest; and (b) four EW phase images taken from the in (a) marked area in four accessible zone axis orientations ( $[1\ 1\ 1]$ ,  $[1\ 1\ 0]$ ,  $[1\ 0\ 1]$ , and  $[0\ 1\ 1]$ ) indicating the defined tilt angles.

has been utilized in a first discrete tilt experiment on a thin area in a gold sample in a high-resolution, highly sensitive environment (UT lens of Berkeley's OAM microscope). Four important low-index zone axis orientations of an only few nanometre wide nanostructure ("bridge") in an ultrathin gold film have been reached (see Fig. 5a). Four EW phase images in Fig. 5b depict the result of our discrete tilt experiment from the area marked in Fig. 5a. They correspond to four accessible zone axis orientations ( $[1\ 1\ 1]$ ,  $[1\ 1\ 0]$ ,  $[1\ 0\ 1]$ , and  $[0\ 1\ 1]$ ). The tilt angles between zone axes ( $35.3^\circ$ ) are indicated in Fig. 5b. In each of these zone axes a focal series of HRTEM images has been recorded to reconstruct the EWF  $\Psi$ . The sample is twisted in the selected region preventing the tomographic reconstruction since no other crystallographic pole could be reached. Thus, a stable holder with wide tilting capabilities is necessary for performing DT in high performance electron microscopes. Clearly, selected regions of thin foils can be reconstructed by DT if a high tilting angle holder can be used, but other approaches are also possible depending on the characteristics of the sample.

### 5.2. Generation of a discrete grid by a phase contrast simulation zone axis tilt experiment

To mimic a discrete tilt experiment on our modelled gold nanocrystal (see Section 4), simulated through focus series are used to determine complex EWFs in six zone axis orientations by image reconstruction. Each EWR has been performed by first simulating 20 lattice images (size  $100 \times 100 \text{ \AA}$ ) for six different zone axis projections ( $[1\ 1\ 1]$ ,  $[1\ 1\ 1]$ ,  $[0\ 0\ 1]$ ,  $[1\ 1\ 0]$ ,  $[1\ 1\ 0]$ , and  $[0\ 1\ 1]$ ) as indicated in Fig. 4b. This is done by using the multislice algorithm in the MacTempas software package [68]. The focus series is started at Lichte defocus [70] ( $\Delta f = -18.9 \text{ nm}$  for  $g_{\max} = 20.0 \text{ nm}^{-1}$ ) with a focus difference between the images of  $0.8 \text{ nm}$ . The assumed microscope parameters [69] are the following: acceleration voltage  $200 \text{ kV}$ ,  $C_s = 0$ , resolution =  $0.05 \text{ nm}$  and sampling rate of  $0.01 \text{ nm/pixel}$  [34,71]. The accuracy of the multislice calculation has been improved by subslicing the nanocrystal structure in order to create at least one projected potential for each atomic layer. The number of layers varies depending on the chosen orientation. There are, for example, nine layers in  $\langle 0\ 0\ 1 \rangle$  (see Fig. 4a where the number of layers can be counted for directions perpendicular to the shown projections) or 17 along  $\langle 1\ 1\ 0 \rangle$  and thus a corresponding number of potentials can be obtained. The number of atoms in each column of the simulated image needs to be determined. In the present case, a direct determination is possible since the atomic positions in a nanocrystalline particle are known a priori. However, in general, such a number can be retrieved by applying the channelling theory [45] as described in more detail elsewhere [33,35]. Figs. 6a and 7a show the amplitude and phase images of  $\Psi$  (the total electron wave) for the  $[0\ 0\ 1]$  and the  $[1\ 1\ 0]$  zone axis orientations, respectively. Figs. 6b and 7b show the corresponding amplitude and phase images of the channelling wave  $\Psi_s$ . Plotting the real and the imaginary part at the column position from  $\Psi_s$  in a channelling map produces Figs. 6c and 7c, respectively. Such a map allows determination of the number of atoms for each particular atomic column. For instance, in the  $\langle 0\ 0\ 1 \rangle$  projection there are up to five atoms in an atomic column of the nanocrystal (see Fig. 6c), and up to nine atoms in  $[1\ 1\ 0]$  (see Fig. 7c). By analyzing all six calculated projections of the nanocrystal, a discrete data grid can be created, i.e., projection data with the column position and the number of atoms in each column.

### 5.3. Discrete tomography reconstruction of the nanocrystal

The 2-D simulation images from the previous section, containing the counted atom data, are used as input for a DT algorithm [17]. In the reconstruction algorithm, it is assumed that atoms in the nanocrystal under consideration are located on a grid point and behave identically [72].

Fig. 8a shows the result of applying the DT algorithm to the data obtained from image simulation. In this case results are presented along  $[0\ 0\ 1]$ . Thus, a series of nine

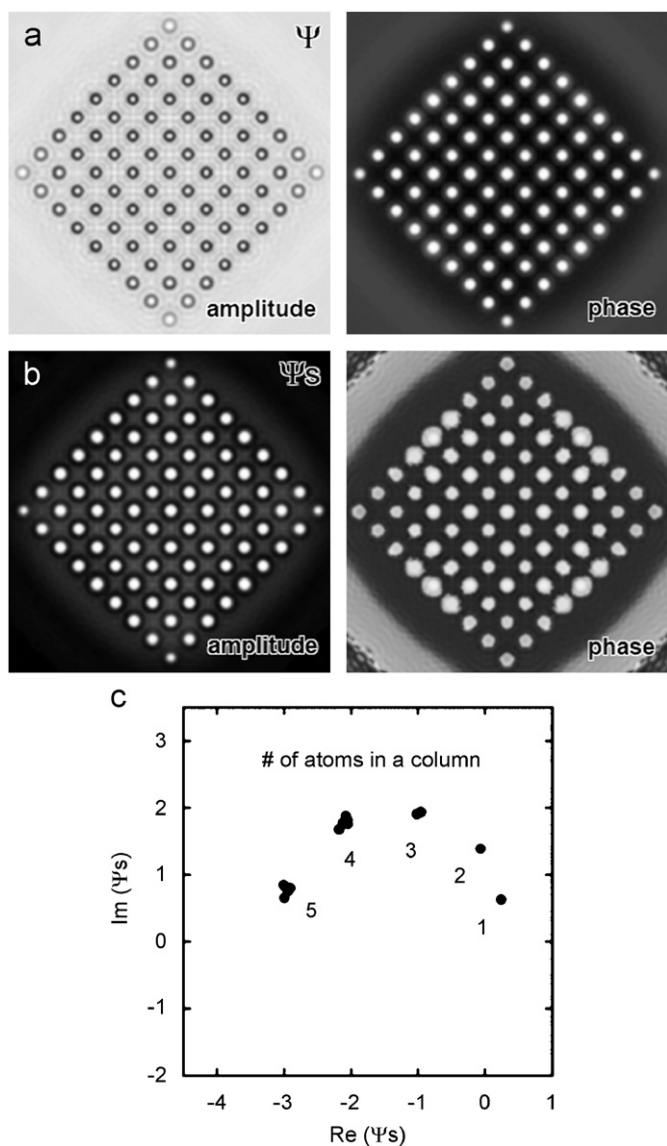


Fig. 6. [001] zone axis orientation; (a) amplitude and phase image of reconstructed exit wave (EW)  $\Psi$ ; (b) amplitude and phase image of the channelling wave  $\Psi_s$ ; and (c) corresponding channelling map (Argand plot) of  $\Psi_s$  values (showing up to five atoms in a column).

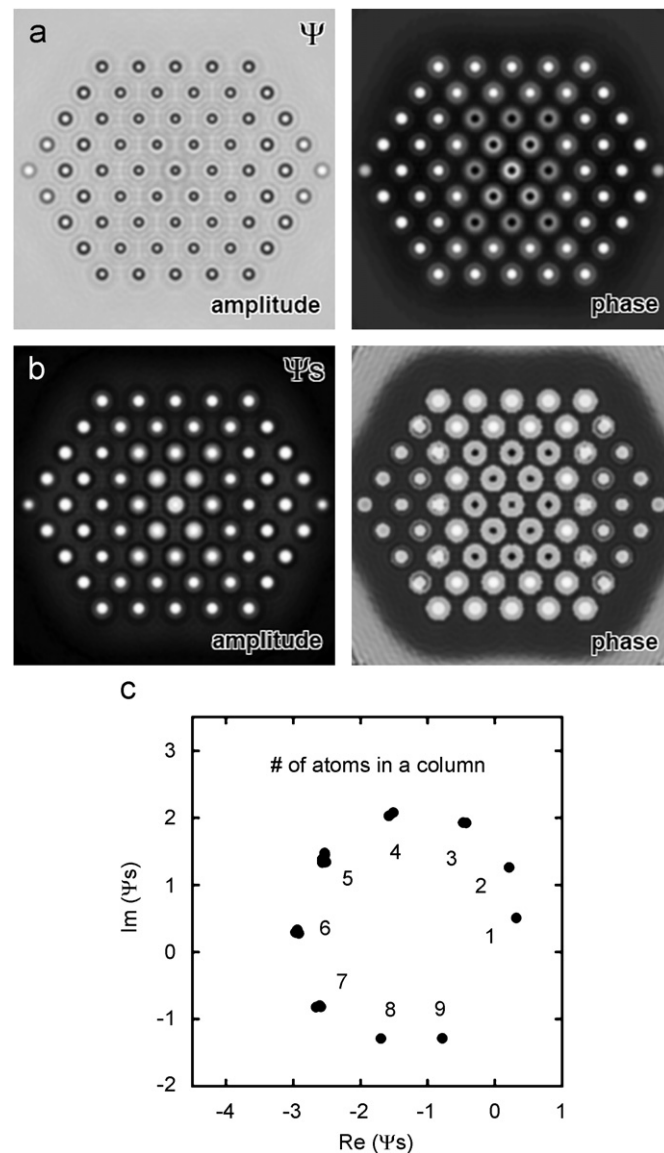


Fig. 7. [110] zone axis orientation; (a) amplitude and phase image of reconstructed exit wave (EW)  $\Psi$ ; (b) amplitude and phase image of the channelling wave  $\Psi_s$ ; and (c) corresponding channelling map (Argand plot) of  $\Psi_s$  values (showing up to nine atoms in a column).

atomic layers are presented as a function of position in the reconstructed nanocrystal. The top layer is shown first and downwards the successive layers are accommodated in the figure. Positions filled by atoms are indicated by means of “X” and dots represent empty positions. Fig. 8b shows the projected potentials of the individual layers for comparison. The potentials are calculated directly from the nanocrystalline particle and had been used for the multislice calculation. As can be seen, the final tomographic result (Fig. 8a) renders the exact position of all 309 atoms of the nanoparticle and thus achieves the 3-D desired reconstruction. The results shown in Fig. 8 have been achieved by using only three projections (i.e., EWRs), along [001], [110] and [110]. This data is already sufficient to recover the position of all atoms in the sample.

The image simulations (see Section 5.2) have also been performed for the [111], [111] and [011] projections, but they have only been used to verify the solution found by the algorithm.

Data from three projections will not be sufficient to guarantee a unique solution in general. In fact, there may still exist several different reconstructions with the same projections even when a large number of projections is available. As an example, Fig. 9a shows a 3-D structure which is not uniquely determined by its projections along the [001], [010] and [100] zone axes (right side of Fig. 9a). A simple exchange of the filled positions with the vacant positions creates a different structure (shown in Fig. 9b), which has the same 2-D projections along the [001], [010] and [100] axis orientations (right side of Fig. 9b).

Fortunately, the occurrence of such structures becomes much less likely when the number of available projections increases.

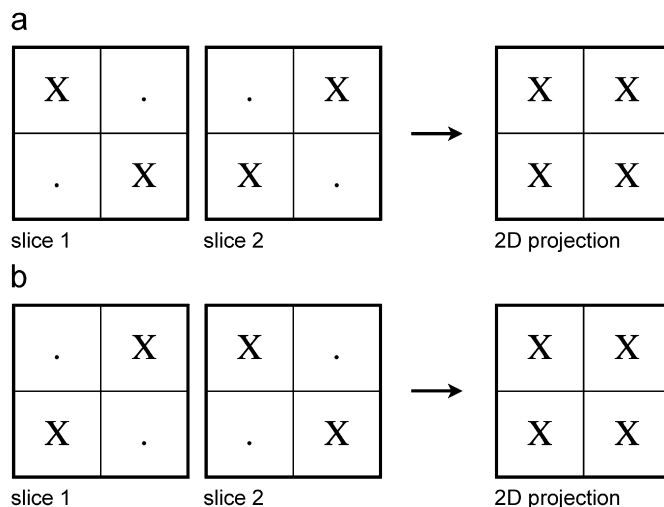
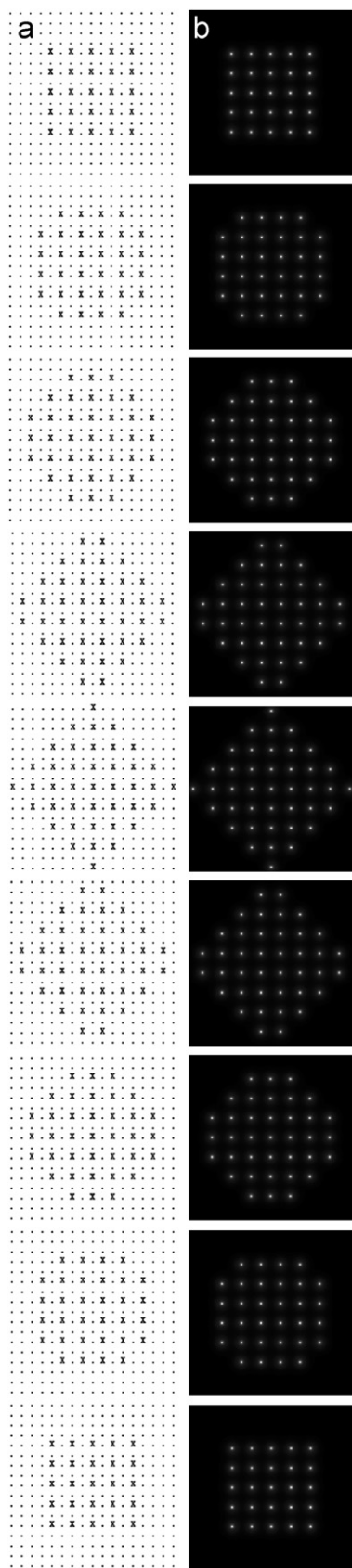


Fig. 9. (a) Cubic 3-D structure consisting of eight potential atom positions (see slice 1). Occupied positions are marked by “X”, vacant positions by “.”. This structure cannot be uniquely determined by its 2-D projections along the [00 1], [0 1 0], and [1 0 0] axis orientations (shown on the right-hand-side). (b) Exchanging the occupied positions with the vacant positions yields a different structure (shown in slice 2), which has the same 2-D projections along the [00 1], [0 1 0], and [1 0 0] axis orientations.

#### 5.4. Consideration of noise level and atom count errors

In this section we first examine the effect of noise in the individual HRTEM images on the ability to count the atoms using the reconstructed EWF. Subsequently, we provide reconstruction results for the case that the atom count data contains a considerable number of count errors. If the sample consists of several different types of atoms, such count errors are likely since an atom of one type can easily be confused with one or more atoms of another type. In the present investigation, the samples consist of a single atom type, but the same approach can also be used in more general cases.

Noise in the acquired images limits the ability to detect a single atom in a given sample column. In real experimental images, noise is always an important factor. Therefore, DT will only be useful if the approach is robust with respect to noise. In the simulation results of the previous section, the number of atoms in each column has been counted and determined perfectly. This is not realistic for an experimental image, which may contain several count errors.

##### 5.4.1. Consideration of Gaussian noise and Poisson noise in HRTEM image simulation

There are several different factors contributing to noise in experimental HRTEM images. Poisson noise occurs

Fig. 8. Final results of the 3-D reconstruction of each position of the 309 atoms in the cube octahedron nanocrystal by discrete tomography. (a) Successive atomic layers (9) of the reconstructed nanocrystal resulting from application of the discrete tomography algorithm. Filled positions (atoms) are marked with “X” and vacant positions with dots. (b) Nine potentials of the atomic layers in the nanocrystal included for comparison. The cube octahedron particle is viewed along a  $\langle 001 \rangle$  zone axis.

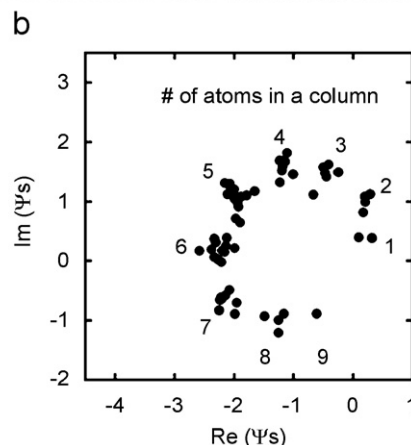
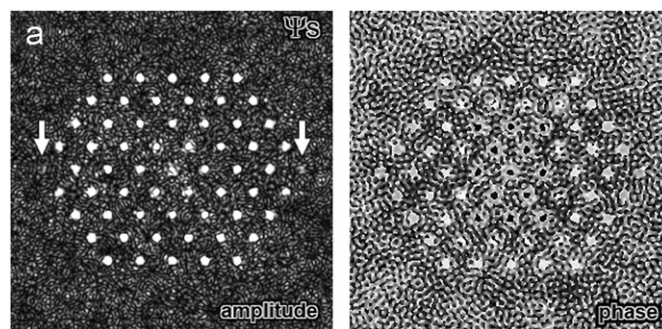
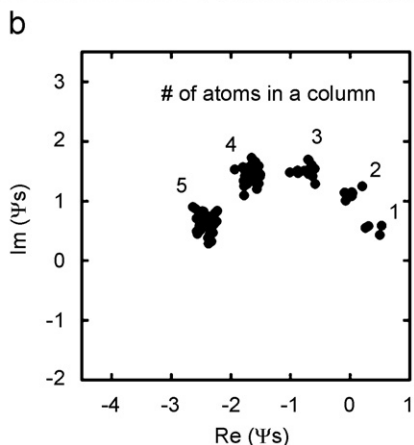
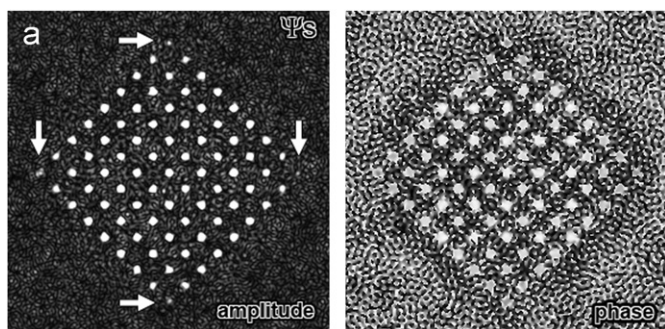


Fig. 10. Consideration of Gaussian noise ( $S/N \sim 1$ ) and Poisson noise in each simulated HRTEM lattice in  $[001]$  zone axis orientation prior exit-wave reconstruction. (a) Amplitude and phase image of channelling wave  $\Psi_S$ -position of atomic columns consisting only of a single atom are marked; and (b) corresponding channelling map of  $\Psi_S$  values—revealing the ability to identify each four single atom columns in a simulation experiment taking large noise values into account.

Fig. 11. Consideration of Gaussian noise ( $S/N \sim 1$ ) and Poisson noise in each simulated HRTEM lattice in  $[110]$  zone axis orientation prior exit-wave reconstruction. (a) Amplitude and phase image of channelling wave  $\Psi_S$ -position of atomic columns consisting only of a single atom are marked; and (b) corresponding channelling map of  $\Psi_S$  values—revealing the ability to identify each two single atom columns in a simulation experiment taking large noise values into account.

due to the stochastic nature of the individual electrons in the electron beam. Its influence can be reduced by increasing the intensity of the electron beam. Thus, the magnitude of Poisson noise is completely determined by the signal in the simulated, noiseless HRTEM image. Additionally, noise can be introduced by imperfections in the CCD camera and in the image recording procedure. In this work, we assume that noise for each camera pixel is independent and follows a Gaussian distribution.

Noise is introduced to the present work by applying both Poisson and Gaussian noise to the HRTEM images prior to the exit wave reconstruction procedure. Each of the HRTEM images in the simulation has an average electron count of 5000 per pixel of the CCD camera. First, we apply Poisson noise to the images. Next, a random value from a Gaussian distribution with  $\lambda = 0$  and  $\sigma = 5000$  is generated for each of the pixels in every image and added to the images containing the Poisson noise. Note that the standard deviation of the noise is equal to the average electron count (i.e.,  $S/N \sim 1$ ). The results for  $[001]$  and  $[110]$  projections are shown in Figs. 10 and 11, respectively.

Figs. 10a and 11a show the amplitude and phase images of the channelling wave  $\Psi_S$  for  $[001]$  and  $[110]$ ,

respectively. The atom columns containing only a single atom are detectable in the channelling wave (marked by arrows), even under the influence of both Poisson noise and Gaussian noise in each HRTEM image. This demonstrates that, under severe noise conditions, the number of atoms in each column can still be counted reasonably well (for comparison see experimental data in Fig. 1). Plotting the real against the imaginary part of  $\Psi_S$  at the column position in a channelling map produces Figs. 10c and 11c for the two orientations under consideration. Again, such a map allows determination of the number of atoms for each particular atomic column. By analyzing all six calculated projections of the nanocrystal, a discrete data grid can be created.

#### 5.4.2. Consideration of “atom count errors” in the discrete tomography algorithm

Depending on the magnitude of the noise, count errors can occur. If, in a projected atom column, there is only a small deviation between the expected (perfect) channelling wave for a certain number of atoms and the measured channelling wave, the atom count can be “rounded” and the (exact) correct value can still be determined. However, if the noise causes a deviation of half the difference

in the channelling wave phase caused by adding one atom in a particular column, a count error occurs in that column.

Fortunately, it may still be possible to compute a perfect reconstruction from the measured projection data if the number of count errors is not too large. If the number of available projections is larger than what would be necessary in the case of perfect data, redundancy in the data can be used to correct count errors. When real-valued quantities are measured in an experiment, repetition of the experiment and averaging the results can reduce the errors, but the number of errors can never be zero. In the present case of measuring discrete quantities, it may be possible to remove the errors completely by using the redundancy in the discrete projection data. Error correction of discrete signals has been studied extensively in the field of Coding Theory [73]. However, it is not obvious how to exploit it in the case of DT.

The algorithm that we used for computing the reconstructions [17] will typically not compute a perfect reconstruction when the projection data contains even just a small number of count errors. However, it is known that its reconstruction result is not very different from the

unknown “original” crystal. A very simple algorithm can be applied as a postprocessing step to improve the reconstruction in case of count errors. Our implementation is a so-called “hill-climb” approach. In each step, the current reconstruction is locally modified to improve its “quality” until no further improvement can be done. (A “local modification” consists of changing a grid position from 0 to 1 or vice versa.) Thereby, the “quality” of a reconstruction is defined as the total deviation of its projections from the measured atom count data.

The “hill-climb” procedure has been tested using perfect projections of the nanocrystal (without count errors, Fig. 4) as the starting point. A number of count errors were added to the projection data by repeatedly selecting a random projected column and adding +1 or -1 (both with 50% probability) to the number of atoms in that particular column. Negative atom counts are not allowed and set to zero.

Fig. 12a summarizes the results for varying numbers of count errors using six zone axis projections. As mentioned in Section 5.3, three projections ( $[001]$ ,  $[110]$ , and  $[1\bar{1}0]$ ) were sufficient to compute a perfect reconstruction from perfect projection data. The three additional projections

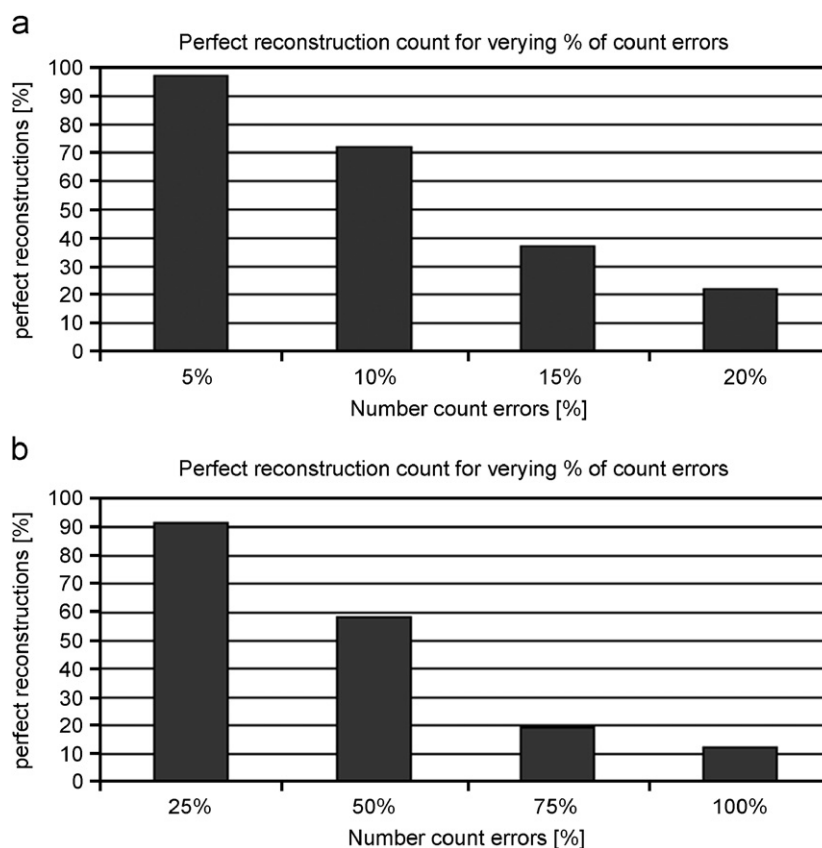


Fig. 12. Success rate in perfect 3-D reconstructions after considering varying numbers of atom count errors by using all six projections. (a) For each percentage of count errors (5%, 10%, 15% and 20% of the total number of atom columns) 100 experiments were performed, each time using a different random distribution of errors. The graph shows the number of times a perfect reconstruction (in %) was obtained. (b) There are 246 columns that contain only three atoms or less. Count errors have been applied to 25%, 50%, 75%, and 100% of those columns. The graph shows the number of times a perfect reconstructions (in %) was obtained in this case by applying 100 test runs.

([1 1 1], [1 1 1] and [0 1 1]) that provide only “redundant” information in case of perfect projections are now essential to correct for errors.

For each percentage of count errors (5%, 10%, 15% and 20% of the total number of atom columns), 100 experiments were performed, each time using a different random distribution of errors (Fig. 12a). The graph in Fig. 12a shows the number of times a perfect reconstruction was obtained. Good results are obtained up to an error count rate of 10% (success rate of 72%). An error count equal to 20% corresponds to a low success rate of the reconstruction (22%). However, such a number of errors can be considered unusually high for a microscope that is capable of detecting single atoms.

Amorphous support layers carrying the nanocrystal or residual aberrations causing delocalization effects at the edge of the nanocrystal can make atom count errors much more likely. This specially affects atoms in columns close to surface layers that contain only a few atoms. Thus additional evaluations have been performed using all six projections accordingly. Count errors have been added exclusively to the 246 columns that contain at most three atoms. In this manner, the algorithm has been tested with 62, 123, 185 and 246 count errors, corresponding to 25%, 50%, 75% and 100% of such columns close or at a free surface. In this particular condition some columns end up with more than one error and others without any count errors. The results are shown in Fig. 12b. There is a success rate of the reconstruction higher than 90% for a relative count error of 25% and it decreases to about 60% when the count error increases to 50%. Such results are very encouraging as to the possible use of the current algorithm for reconstruction on the basis of experimental images.

Summarizing, the present results demonstrate that the algorithm is well capable of correcting count errors or noise. Additionally, the number of projections used here is very small in comparison to other common algorithms for tomography. Increasing the number of projections significantly increases the tolerable number (percentage) of errors. Thus, increasing the number of experimentally determined projections can still be attempted.

### 5.5. Consideration of defects: variations from the discrete grid

So far we have focused our attention to utilize atomic resolution electron tomography as a 3-D visualization tool on perfect crystals—i.e., atoms are properly aligned on the lattice—to directly explore size and shape information on the sub-nanometre scale. The ability to compute such reconstructions would be an important step towards reliable correlation of size- and shape-dependent properties of nanocrystals.

However, it is also important to deal with deviations from the regular lattice caused by defects. In this section, we consider experiments with missing atoms, both on the

surface and in the core of the nanocrystal to test if our approach allows the detection of vacancies with equal (atomic) resolution in all three spatial dimensions. To the best of our knowledge, no other methods are currently capable of providing such detailed information.

Subsequently, we briefly discuss how our approach could be extended to deal with other types of defects, such as dislocations and stacking faults, as part of our ongoing research.

#### 5.5.1. Defective nanocrystal: missing atoms on surface and consideration of a cavity

The simulation experiments from Section 5.2—this time using a “defective” gold nanocrystal test structure with only 300 atoms—have been repeated to examine the stability of our approach in case of defects such as surface steps and vacancies. The “defective” test structure is shown in Fig. 13; nine missing atoms (four on the surface, one in an isolated vacancy and four in a cavity at the centre of the particle) are illustrated as darker spheres. Again, we applied both Poisson noise and Gaussian noise ( $S/N \sim 1$ ) to each of the simulated HRTEM images to simulate realistic experimental noise conditions.

Figs. 14 and 15 show the amplitude and phase images and the corresponding channelling maps for the [0 0 1] and [1 1 0] projections, respectively. The atom columns containing only a single atom and a missing atom at the surface are clearly visible in the channelling wave (marked by arrows and a circle, respectively). Again, by analyzing all six calculated projections of the nanocrystal, a discrete data grid can be created. The figures demonstrate that it is possible to count the number of atoms in each column reasonably well even in consideration of missing atoms (defects) and under severe noise conditions.

The result of the reconstruction is shown in Fig. 16—nine atomic layers in [0 0 1] projection after applying the DT algorithm to the data obtained from image simulation in Fig. 16a and the corresponding projected potentials that have been used for the multislice calculations in Fig. 16b. Positions filled by atoms are indicated by means of “X”

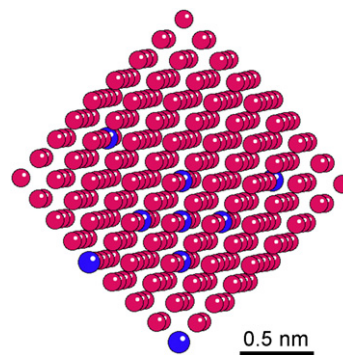


Fig. 13. Consideration of simple defects in the atomic structure of the nanocrystal used for image simulation. It consists of “only” 300 atoms and the nine (9) in the image simulation neglected atoms at the surface and inside the crystal (cavity) are indicated by larger size and darker colour.

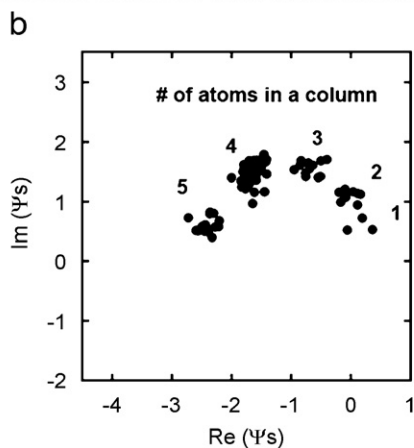
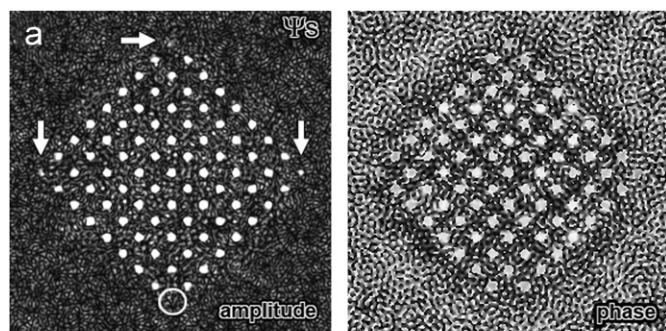


Fig. 14. Consideration of simple defects in the atomic structure of the nanocrystal (nine missing atoms at the surface and inside the crystal) + -Gaussian noise ( $S/N \sim 1$ ) and Poisson noise in each simulated HRTEM lattice in  $[001]$  zone axis orientation prior exit-wave reconstruction. (a) Amplitude and phase image of channelling wave  $\Psi_s$ -position of atomic columns consisting only of a single atom are marked by arrows, position of a missing single atom column is marked by "O"; and (b) corresponding channelling map of  $\Psi_s$  values.

and dots represent empty positions. The final tomographic result renders the exact position of all 300 atoms of the "defective" gold nanocrystal and thus achieves the desired reconstruction even of the vacancies in 3-D.

This clearly demonstrates that in the case of several missing atoms the channelling map can still be used effectively to count the number of atoms in each column. From the atom count data in the six zone axis orientations we were able to compute a perfect reconstruction of the original nanocrystal by DT. The results show that our DT approach has the ability to reconstruct nanocrystals containing vacancies, or even cavities consisting of several atoms in 3-D. It has been shown that if the projection data are sufficiently accurate, vacant position buried deeply inside complex shaped structures can be reconstructed [18]. Of course, one requirement for reconstructing defect structures is that the atom counting step can still be performed accurately, i.e., by utilizing electron channelling based crystallography [35].

### 5.5.2. Defective nanocrystal: consideration of more complex defect structures

Another important aspect, how to extend the approach to samples that contain other types of defect structures

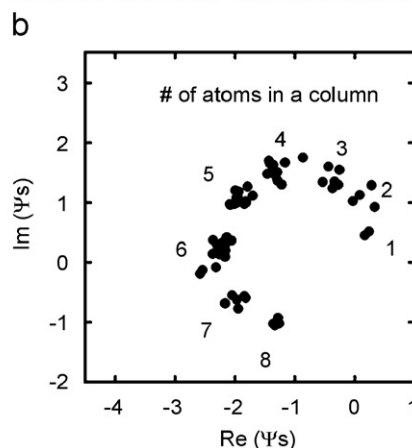
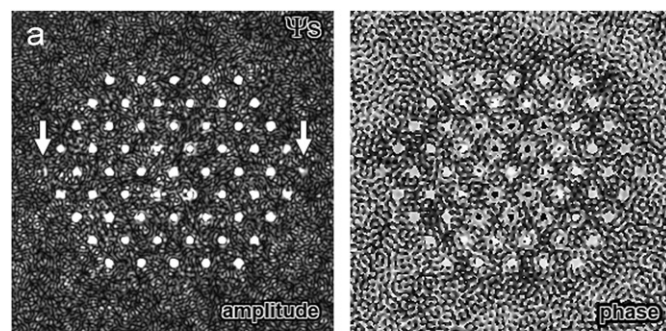


Fig. 15. Consideration of simple defects in the atomic structure of the nanocrystal (nine missing atoms at the surface and inside the crystal) + -Gaussian noise ( $S/N \sim 1$ ) and Poisson noise in each simulated HRTEM lattice in  $[110]$  zone axis orientation prior exit-wave reconstruction. (a) Amplitude and phase image of channelling wave  $\Psi_s$ -position of atomic columns consisting only of a single atom are marked by arrows; and (b) corresponding channelling map of  $\Psi_s$  values.

such as dislocations, stacking faults, twin boundaries, is part of our ongoing research and will be addressed in a future publication. The main difficulty of such defects is that in certain orientations the atoms do not project as "straight columns" that allow for counting of the number of atoms utilizing the channelling approach. However, important information about the location of such defects can often be obtained by visual inspection of the projection images. One idea is to use this information in the reconstruction algorithm by splitting the reconstruction grid into several partial grids and assuming a regular grid for the reconstruction of each of the parts.

### 5.5.3. Nanocrystals that contain several different types of atoms

Our approach can be used for nanocrystals that contain several different types of atoms as well, provided that it is possible to count the atoms of each type independently. Recent progress in reverse multislice calculations [46,47], based on the reconstructed electron exit wave, allows for counting the number of atoms of each element in every column of the projected nanocrystal.

Separate reconstructions can be computed for each of the atom types, indicating in which grid position an atom

of that particular type is present. The resulting reconstructions for each of the atom types can then be merged, resulting in a reconstruction of the complete nanocrystal. If

each of the partial reconstructions can be computed accurately, this procedure will yield a correct result.

## 6. Conclusion

Using the fact that the nature of a crystal is discrete on an atomic scale as prior knowledge for the reconstruction algorithm simplifies the reconstruction problem and drastically reduces the required input data. Using 2-D high-resolution electron microscope images, data from less than 10 projections are often sufficient.

The improved sensitivity in electron microscopy to detect single atoms in a column, already shown in experiments [52,54] and here mimicked by image simulations, makes this novel approach of electron tomography feasible. It involves only the consideration of a discrete grid of atoms in a crystal. We applied this technique to the reconstruction of a nanocrystalline particle where the atoms are arranged in a known and highly regular grid. It was shown that by using the knowledge of atomicity, accurate atomic resolution 3-D tomograms can be computed with a much reduced amount of data. Only three projections were necessary to determine the nanoparticle shape and position of all atoms.

Simulation of data in six zone axis projections poses no particular difficulty. Experimentally, however, the restriction at the moment is the availability of suitable holders. A newly designed dual-axes tomography holder will be developed in the framework of the TEAM-project [69]. This will enable the performance of the “real” experiment. Based on our simulation experiments we expect that it will present, for the first time, an atomic resolved tomographic reconstruction.

Nevertheless, a special double-tilt tomography holder (H. Zandbergen, TU Delft/NL, 2005) has been utilized in a first discrete tilt experiment in a high-resolution, highly sensitive environment (UT lens of Berkeley’s OAM microscope). The experiment demonstrated that it is feasible to acquire zone-axis projection images of a single nanocrystal from different angles.

Defects have been considered by testing the approach in the case of missing atoms—on the surface, as an isolated vacancy and in a cavity—to the best of our knowledge not possible to detect by currently available tomographic algorithms. In future research we will consider the incorporation of more complex defects into the DT model.

In all simulations experiments, noise conditions have been actualized by applying both Poisson noise and

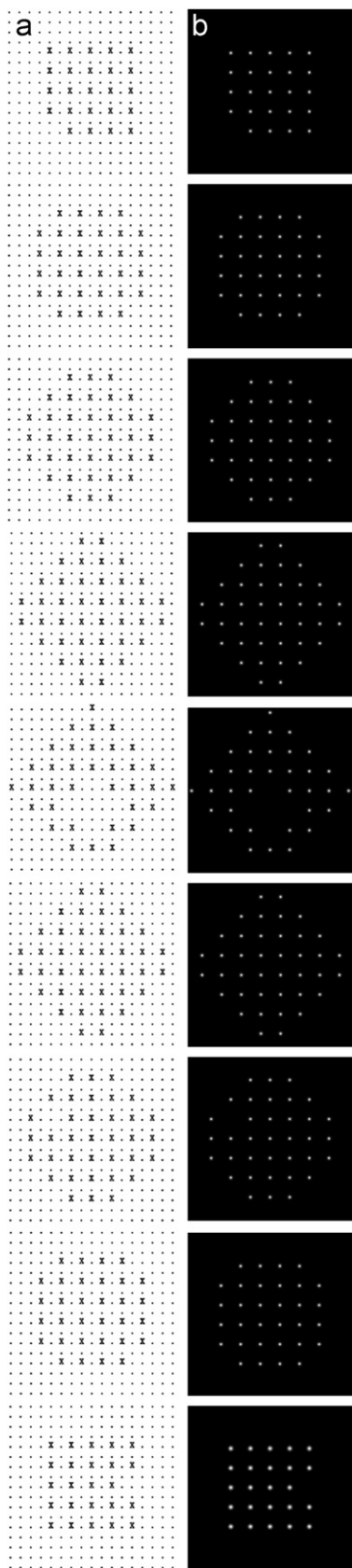


Fig. 16. Final results of the 3-D reconstruction of each position of the 300 atoms in the cube octahedron nanocrystal (nine missing atoms in comparison to Fig. 6) by discrete tomography. (a) Successive atomic layers (9) of the reconstructed nanocrystal resulting from application of the discrete tomography algorithm. Filled positions (atoms) are marked with “X” and vacant positions with dots. (b) Nine potentials of the atomic layers in the nanocrystal included for comparison. The cube octahedron particle is viewed along a  $\langle 001 \rangle$  zone axis.

Gaussian noise in each HRTEM image. The number of atoms in each column can still be counted with reasonable accuracy under extreme noise conditions.

Even more, if the atom count data contains a considerable number of count errors, due to noise or other sources of experimental errors, it may still be possible to compute a perfect reconstruction. For a number of count errors that equals 10% of the total number of atom columns, perfect results were obtained in 72% of the reconstructions in our simulation experiments.

An important advantage of DT is its ability to provide information about positions of all atoms including those in the core of nanocrystals. These atoms are always concealed by many other atoms in projection images. Our approach allows the detection in 3-D of vacancies with equal (atomic) resolution in all three spatial dimensions. To the best of our knowledge, no other methods are currently capable of providing such detailed information.

### Acknowledgements

The authors acknowledge support of the National Center for Electron Microscopy (NCEM), Lawrence Berkeley National Lab (LBNL), which is supported by the US Department of Energy under contract no. DE-AC02-05CH11231. The authors would like to thank especially Prof. Dr. Henny Zandbergen (NCHREM, TU Delft, NL) and ChengYu Song (NCEM, LBNL Berkeley, CA). J.R. Jinschek acknowledges support of ICTAS/Virginia Tech and was partly supported by a Feodor-Lynen-Fellowship of the Alexander-von-Humboldt Foundation, Bonn/Germany. K.J. Batenburg is supported by FWO, Belgium under contract no. G.0247.08. H.A. Calderon acknowledges support from IPN and CONACYT.

### References

- [1] P.A. Midgley, M. Weyland, J.M. Thomas, B.F.G. Johnson, *Chem. Commun.* (10) (2001) 907.
- [2] M. Weyland, P.A. Midgley, J.M. Thomas, *J. Phys. Chem. B* 105 (33) (2001) 7882.
- [3] I. Arslan, T.J. Yates, N.D. Browning, P.A. Midgley, *Science* 309 (5744) (2005) 2195.
- [4] M. Weyland, T.J. Yates, R.E. Dunin-Borkowski, L. Laffont, P.A. Midgley, *Scripta Mater.* 55 (1) (2006) 29.
- [5] S. Bals, G. Van Tendeloo, C. Kisielowski, *Adv. Mater.* 18 (7) (2006) 892.
- [6] I. Arslan, J.R. Tong, P.A. Midgley, *Ultramicroscopy* 106 (11–12) (2006) 994.
- [7] P. Gilbert, *J. Theor. Biol.* 36 (1) (1972) 105.
- [8] A.C. Kak, M. Slaney, *Classics Appl. Math.* 33 (2001) 1.
- [9] J.R. Tong, I. Arslan, P.A. Midgley, *J. Struct. Biol.* 153 (1) (2006) 55.
- [10] H.-R. Wenk, K.H. Downing, M. Hu, M.A. O’Keefe, *Acta Crystallogr. A* 48 (5) (1992) 700.
- [11] S. Bals, C.F. Kisielowski, M. Croitoru, G. Van Tendeloo, *Microsc. Microanal.* 11 (Suppl. 2) (2005) 2119.
- [12] W. Hoppe, *Naturwissenschaften* 61 (6) (1974) 239.
- [13] W. Hoppe, B. Grill, *Ultramicroscopy* 2 (2–3) (1977) 153.
- [14] J. Miao, T. Ohsuna, O. Terasaki, K.O. Hodgson, M.A. O’Keefe, *Phys. Rev. Lett.* 89 (15) (2002) 155502.
- [15] J.S. Wu, U. Weierstall, J.C.H. Spence, *Nat. Mater.* 4 (2005) 912.
- [16] J.M. Zuo, I. Vartanyants, M. Gao, R. Zhang, L.A. Nagahara, *Science* 300 (5624) (2003) 1419.
- [17] K.J. Batenburg, *Electron. Notes Discr. Math.* 20 (2005) 247.
- [18] K.J. Batenburg, *J. Math. Imag. Vision*, online (doi:10.1007/s10851-006-9798-2), 2006.
- [19] G.T. Herman, A. Kuba, *Discrete Tomography—Foundations, Algorithms, and Applications*, A Birkhäuser book, Boston, 1999.
- [20] G.T. Herman, A. Kuba, *Advances in Discrete Tomography and its Applications*, A Birkhäuser book, Boston, 2007.
- [21] A. Ourmazd, D.W. Taylor, M. Bode, Y. Kim, *Science* 246 (4937) (1989) 1571.
- [22] C. Kisielowski, P. Schwander, F.H. Baumann, M. Seibt, Y. Kim, A. Ourmazd, *Ultramicroscopy* 58 (2) (1995) 131.
- [23] P. Schwander, C. Kisielowski, M. Seibt, F.H. Baumann, Y. Kim, A. Ourmazd, *Phys. Rev. Lett.* 71 (25) (1993) 4150.
- [24] B. Freitag, S. Kujawa, P.M. Mul, J. Ringnalda, P.C. Tiemeijer, *Ultramicroscopy* 102 (3) (2005) 209.
- [25] P.E. Batson, N. Dellby, O.L. Krivanek, *Nature* 418 (6898) (2002) 617.
- [26] M. Haider, S. Uhlemann, S.E.H. Rose, B. Kabius, K. Urban, *Nature* 392 (1998) 768.
- [27] W. Coene, A. Thust, M. Op de Beeck, D. Van Dyck, *Ultramicroscopy* 64 (1–4) (1996) 109.
- [28] A. Thust, W.M.J. Coene, M. Op de Beeck, D. Van Dyck, *Ultramicroscopy* 64 (1–4) (1996) 211.
- [29] R.R. Meyer, J. Sloan, R.E. Dunin-Borkowski, A.I. Kirkland, M.C. Novotny, S.R. Bailey, J.L. Hutchison, M.L. Green, *Science* 289 (5483) (2000) 1324.
- [30] J.R. Jinschek, C. Kisielowski, M. Lentzen, K. Urban, *Microsc. Microanal.* 8 (S02) (2002) 466.
- [31] J.R. Jinschek, C. Kisielowski, T. Radetic, U. Dahmen, M. Lentzen, A. Thust, K. Urban, *Mater. Res. Soc. Symp. Proc.* 727 (2002) R1.3.1–6.
- [32] C. Kisielowski, J.R. Jinschek, *Phys. Microstruct. Semicond.* 27 (2002) 137.
- [33] J.R. Jinschek, C. Kisielowski, D. Van Dyck, P. Geuens, in: I.T. Ferguson, N. Narendran, S.P. DenBaars, J.C. Carrano (Eds.), *Proceedings of SPIE*, vol. 5187, SPIE, Bellingham, WA, 2004, pp. 54–63.
- [34] J.R. Jinschek, K.J. Batenburg, H.A. Calderon, R. Kilaas, V. Radmilovic, C. Kisielowski, *Microsc. Microanal.* 12 (S02) (2006) 1566.
- [35] S. Van Aert, P. Geuens, D. Van Dyck, C. Kisielowski, J.R. Jinschek, *Ultramicroscopy* 107 (6–7) (2007) 551.
- [36] M. Lentzen, K. Urban, *Acta Crystallogr. A* 56 (3) (2000) 235.
- [37] W. Coene, G. Janssen, M. Op de Beeck, D. Van Dyck, *Phys. Rev. Lett.* 69 (26) (1992) 3743.
- [38] D. Van Dyck, M. Op de Beeck, W. Coene, *Optik* 93 (3) (1993) 103.
- [39] A.I. Kirkland, W.O. Saxton, K.-L. Chau, K. Tsuno, M. Kawasaki, *Ultramicroscopy* 57 (4) (1995) 355.
- [40] A.I. Kirkland, W.O. Saxton, G. Chand, *J. Electron. Microsc. (Tokyo)* 46 (1) (1997) 11.
- [41] H. Lichte, *Advances in Optical and Electron Microscopy*, vol. 12, Academic Press, London, 1991, pp. 25–91.
- [42] A. Thust, M.H.F. Overwijk, W. Coene, M. Lentzen, *Ultramicroscopy* 64 (1–4) (1996) 249.
- [43] D. Tang, H.W. Zandbergen, J. Jansen, M. Op de Beeck, D. Van Dyck, *Ultramicroscopy* 64 (1–4) (1996) 265.
- [44] C. Kisielowski, C.J. Hetherington, Y.C. Wang, R. Kilaas, M.A. O’Keefe, A. Thust, *Ultramicroscopy* 89 (4) (2001) 243.
- [45] D. Van Dyck, M. Op de Beeck, *Ultramicroscopy* 1996 (1–4) (1996) 99.
- [46] F.-R. Chen, C. Kisielowski, J.R. Jinschek, J. Plitzko, J.-J. Kai, *Microsc. Microanal.* 10 (S03) (2004) 64.
- [47] F.R. Chen, C. Kisielowski, J.R. Jinschek, J. Plitzko, J.J. Kai, *Microsc. Microanal.* 11 (S02) (2005) 2156.

- [48] P. Geuens, D. Van Dyck, *Ultramicroscopy* 93 (3–4) (2002) 179.
- [49] D. Van Dyck, P. Geuens, J.R. Jinschek, C. Kisielowski, in: *Proceedings International Workshop on Noncrystallographic Phase Retrieval*, Cairns, Australia, 2003.
- [50] W. Sinkler, L.D. Marks, *Ultramicroscopy* 75 (4) (1999) 251.
- [51] D. Van Dyck, P. Geuens, J.R. Jinschek, C. Kisielowski, in: *Proceedings of the 9th Frontiers of Electron Microscopy in Materials Science Conference, FEMMS 2003*, Claremont Resort and Spa in Berkeley, CA, USA, 2003.
- [52] C.L. Jia, K. Urban, *Science* 303 (5666) (2004) 2001.
- [53] A.V. Crewe, J. Wall, J. Langmore, *Science* 168 (3937) (1970) 1338.
- [54] P.M. Voyles, D.A. Muller, J.L. Grazul, P.H. Citrin, H.J. Gossmann, *Nature* 416 (6883) (2002) 826.
- [55] K. van Benthem, A.R. Lupini, M. Kim, H.S. Baik, S. Doh, J.-H. Lee, M.P. Oxley, S.D. Findlay, L.J. Allen, J.T. Luck, S.J. Pennycook, *Appl. Phys. Lett.* 87 (2005) 034104.
- [56] R.J. Gardner, P. Gritzmann, D. Prangenberg, *Discrete Math.* 202 (1–3) (1999) 45.
- [57] P. Fishburn, P. Schwander, L. Shepp, R.J. Vanderbei, *Discrete Appl. Math.* 75 (1) (1997) 39.
- [58] L. Haijdu, R. Tijdeman, *Lin. Alg. Appl.* 339 (1–3) (2001) 147.
- [59] K.J. Batenburg, CWI Report PNA-E0418, 2004.
- [60] Z.L. Wang, *J. Phys. Chem. B* 104 (6) (2000) 1153.
- [61] P. Buffat, J.-P. Borel, *Phys. Rev. A* 13 (6) (1976) 2287.
- [62] M.B. Mohamed, Z.L. Wang, M.A. El-Sayed, *J. Phys. Chem. A* 103 (49) (1999) 10255.
- [63] A.S. Barnard, X.M. Lin, L.A. Curtiss, *J. Phys. Chem. B* 109 (51) (2005) 24465.
- [64] A.S. Barnard, L.A. Curtiss, *ChemPhysChem* 7 (7) (2006) 1544.
- [65] J.A. Ascencio, M. Pérez, M. José-Yacamán, *Surf. Sci.* 447 (1–3) (1999) 73.
- [66] J.-O. Malm, M.A. O’Keefe, *Ultramicroscopy* 68 (1) (1996) 13.
- [67] V. Radmilovic, M.A. O’Keefe, R. Kilaas, in: *Proceedings of the 11th European Congress on Electron Microscopy (EUREM 11)*, 1996, pp. 11–12.
- [68] RKCS, <<http://www.totalresolution.com>>.
- [69] TEAM-project, <<http://ncem.lbl.gov/TEAM-project/index.html>>.
- [70] H. Lichte, *Ultramicroscopy* 38 (1) (1991) 13.
- [71] J.R. Jinschek, H.A. Calderon, K.J. Batenburg, V. Radmilovic, C. Kisielowski, *Mater. Res. Soc. Symp. Proc.* 839 (2005) P4.5.1-6.
- [72] K.J. Batenburg, J.R. Jinschek, H.A. Calderon, C. Kisielowski, *Microsc. Microanal.* 12 (S02) (2006) 1572.
- [73] J.H. van Lint, *Introduction to Coding Theory*, Springer, New York, 1999.